Energy & Environmental Science

A new family of cation-disordered Zn(Cu)-Si-P compounds as high-performance anodes for next-generation Li-ion batteries

Journal:	*Energy & Environmental Science*
Manuscript ID	EE-ART-03-2019-000953.R1
Article Type:	Paper
Date Submitted by the Author:	06-May-2019

Complete List of Authors:	Li, Wenwu; Guangdong University of Technology, School of Materials and Energy; Georgia Institute of Technology, School of Materials Science & Engineering Li, Xinwei; Southern university of science and technology, Liao, Jun; Guangdong University of Technology, Guangzhou 51006, China., School of Materials and Energy Zhao, Bote; Georgia Institute of Technology, School of Materials Science & Engr Zhang, Lei; Georgia Institute of Technology, School of Materials Science and Engineering Huang, Le; Guangdong University of Technology, Liu, Guoping; School of Materials and Energy, Guangdong University of Technology Guo, Zaiping; University of Wollongong, Liu, Meilin; Georgia Institute of Technology, School of Materials Science and Engineering

Journal Name ARTICLE

A new family of cation-disordered Zn(Cu)-Si-P compounds as high-performance anodes for next-generation Li-ion batteries

Received 00th January 20xx,
Accepted 00th January 20xx

DOI: 10.1039/x0xx00000x

www.rsc.org/

Wenwu Li,[a,b] Xinwei Li,*[,c] Jun Liao,[a] Bote Zhao,[b] Lei Zhang,[b] Le Huang,[a] Guoping Liu,[a] Zaiping Guo[d] and Meilin Liu*[,b]

The development of low-cost, high-performance anode materials for Li-ion batteries (LIBs) is imperative to meeting the ever-increasing demands for advanced power sources. Here we report our findings in design, synthesis, and characterization of a new cation-disordered $ZnSiP_2$ anode. When tested in LIBs, the disordered phase of $ZnSiP_2$ demonstrates faster reaction kinetics and higher energy efficiency than the cation-ordered phase of $ZnSiP_2$. The superior performance is attributed to the greater electronic and ionic conductivity and better tolerance against volume variation during cycling, as confirmed by theoretical calculations and experimental measurements. Moreover, the cation-disordered $ZnSiP_2$/C composite exhibits excellent cycle stability and superior rate capability. The performance surpasses all reported multi-phase anodes studied. Further, a number of the cation-disordered phases in the Zn(Cu)-Si-P family with a wide range of cation ratios show similar performances, achieving large specific capacities and high first-cycle Coulombic efficiency while maintaining desirable working potentials for enhanced safety.

Introduction

Li-ion batteries (LIBs) are becoming a highly promising power source for many emerging technologies, including electric vehicles and smart grids.[1-6] To meet the ever-increasing demands, it is imperative to develop low-cost anode materials of high performances: high initial Coulombic efficiency, large specific capacity, suitable working potential for safe operation, high-rate capability, and long-cycling life. Si-based anodes have attracted much attention since it has potential to replace the commercial grade graphite, benefiting from ultra-high gravimetric capacity (with a theoretical capacity of 4200 mA h g^{-1}, 11 times larger than that of a state-of-the-art graphite anode), low working potential, natural abundance in the crust of the earth, and matured processing infrastructure.[7-13] However, the applicability of Si is limited by its low electronic and ionic conductivity and poor mechanical integrity due to large volume change during the lithiation/delithiation process. As a result, micro-sized Si anodes suffer from severe degradation in performance during cycling. To develop a robust electrode architecture with reliable electrochemical Li-storage performances, nanostructure engineering strategies have been applied to synthesize various advanced electrode architecture.[14-15] Unfortunately, the sophisticated synthesis processes and low yield significantly increase the cost of Si-based batteries (cost per watt-hour, $/Wh), thus limiting the practical applications of Si-based electrodes. Red P has also attracted considerable attention as an emerging anode material for rechargeable Li-, Na-, or K-ion batteries (with theoretical capacity of 2,596 mA h g^{-1} corresponding to $Li/Na/K_3P$). However, the low electronic and ionic conductivity hinders its real application.[16-19] To address this problem, various phosphor-carbon composites were proposed, e.g. red P/carbon nanotubes and amorphous P/carbon composite, where carbon matrix serves as the current collector and mechanical-reinforcement backbone.[20-24] However, synthesis of P/C composites often involves wet chemical methods, which require toxic P solvents and produce flammable white P.

Emerging strategy for creating synergistic effects between phases within a multi-phase composite has attracted some attention recently.[25-31] For example, it has been reported that Fe/Co/Ni-SnO_2-graphite[25] and Sn_4P_3-SnSb-Sn[26] composites displayed better cycling stability and higher initial Coulombic efficiency than those with only one or two phases. Compared to the multi-phase composites, a single-phase ternary compound (e.g., Bi_2MoO_6) could achieve much better electrochemical performances in a Li-ion battery due to atomic-level interface engineering and electric-field effect.[32-33] Similar synergistic effects were also reported for other ternary oxides and sulfides because of electrochemically derived multi-phase products.[34-36] However, these ternary compounds usually show compromised electrochemical performance since each electrochemically derived product may have distinctly different multi-step redox reaction mechanism. Additionally, the working potentials of ternary oxide and sulfide anodes are mainly above 1.0 V, resulting in low energy density. Also, it is challenging to synthesize these ternary compounds due to their limited thermodynamic stability. Therefore, rational design of ternary compounds with right chemistry and proper working potentials requires a fundamental understanding of the structure-property relationship, which is urgent and crucial to the development of new battery technologies.

[a] School of Materials and Energy, Guangdong University of Technology, Guangzhou 51006, China.
[b] School of Materials Science and Engineering, Georgia Institute of Technology, Atlanta, Georgia 30332, USA.
[c] Department of Mechanical and Energy Engineering, Southern University of Science and Technology, Shenzhen, 518071, China.
[d] Institute for Superconducting and Electronic Materials, School of Mechanical, Materials and Mechatronics Engineering, University of Wollongong, North Wollongong, NSW 2500, Australia.
* Corresponding authors, E-mail: lixw@sustech.edu.cn; meilin.liu@mse.gatech.edu
Electronic Supplementary Information (ESI) available: [details of any supplementary information available should be included here]. See DOI: 10.1039/x0xx00000x

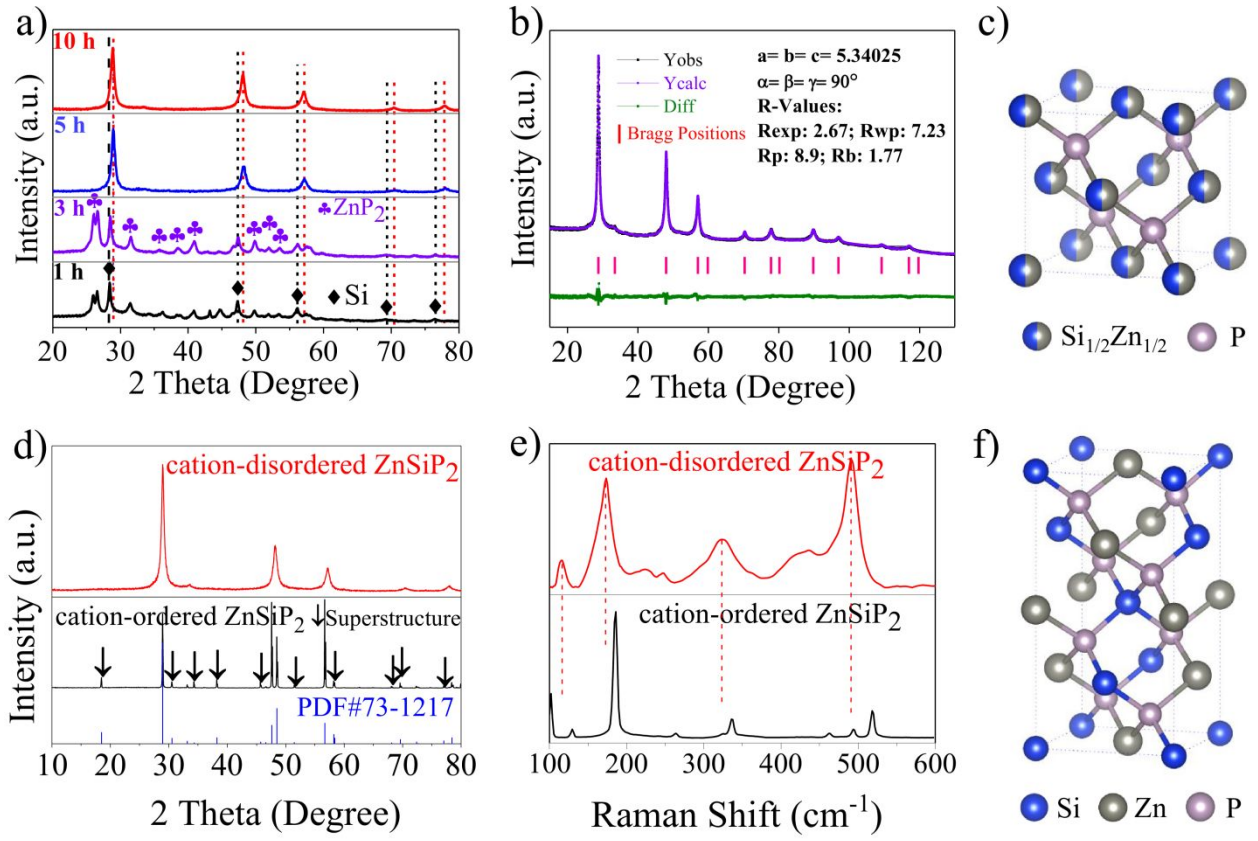

Figure 1. a) Evolution of the XRD patterns for a mixture of Zn-Si-P with a molar ratio of 1: 1: 2 as a function of ball milling time; b) the XRD pattern for the Rietveld structure analysis of the stoichiometric cation-disordered $ZnSiP_2$; c) a schematic crystal structure for the cation-disordered $ZnSiP_2$; d) the XRD patterns of the cation-ordered $ZnSiP_2$ and cation-disordered $ZnSiP_2$; e) the Raman spectra of the cation-ordered $ZnSiP_2$ and the cation-disordered $ZnSiP_2$; f) a schematic crystal structure of the cation-ordered $ZnSiP_2$.

In this article, we reported our finding in design and synthesis of a cation-disordered $ZnSiP_2$ compound as a new-generation anode for LIBs. P and Zn were introduced into the structure of Si by virtue of their similar atomic sizes, bonding characteristics and electronegativity. The as-synthesized compound has a cation-disordered zinc-blend or diamond-like structure, in which the introduced P and Si partially replace S sites and Zn sites, respectively, as confirmed by XRD refinement. The cation-disordered $ZnSiP_2$ anode delivered superior Li-storage properties compared to the cation-ordered $ZnSiP_2$ in terms of reaction kinetics, energy efficiency and cycling stability. The superiority was attributed to higher electronic and ionic conductivity as well as better resistance to volume change during cycling, as confirmed by first-principles calculations and electrochemical impedance spectroscopy. Furthermore, the cation-disordered $ZnSiP_2$ anode demonstrated an intriguing Li-storage mechanism with a peculiar reversibility back to its initial atomistic structure, as confirmed by ex-situ XRD, TEM, Raman, XPS, and electrochemical analysis. By further mixing with carbon, the resulting composite displayed impressive cycling performance with a specific capacity of 1,789 mA h g^{-1} after 700 cycles at 200 mA g^{-1}, and a superior rate capability with a capacity of 585 mA h g^{-1} at a current density of 30 A g^{-1}. These excellent Li-storage performances are attributed to the excellent structural reversibility, fast Li-ion and electron transportation and the unique Li-storage mechanism. Furthermore, many compositions in the Zn(Cu)-Si-P family with various cation ratios displayed similar properties to those of the cation-disordered $ZnSiP_2$, including high initial Coulombic efficiency, large capacity, and proper working potential between P/C and Si anodes.

The cation-ordered tetragonal phase $ZnSiP_2$, a typical ternary II-IV-V2 semiconductor, is widely used in optoelectronics, spintronics, and quantum electronics.[37-39] Nevertheless, its synthesis still adopts the complex and energy-consuming chemical vapor transport (CVT) and electrochemical synthesis method at about 1000 °C. In our study, we have successfully synthesized a new cation-disordered $ZnSiP_2$ phase with Sphalerite structure in high yield by a facile mechanical ball milling process from the corresponding elemental powders as the raw materials. To investigate the phase evolution during the ball milling process, X-ray diffraction was performed to analyze the samples prepared with different milling time. As shown in **Figure 1a**, after milling for 3 h, the main characteristic diffraction peaks of the sample can be assigned to ZnP_2, regardless of some residual Si raw material. After milling for 5 h, the peaks of the intermediate ZnP_2 and remaining Si raw material completely disappeared. All the observed peaks could be assigned to a Si-like structure with all the fingerprint peaks slightly shifted to higher 2 theta positions, compared to that of

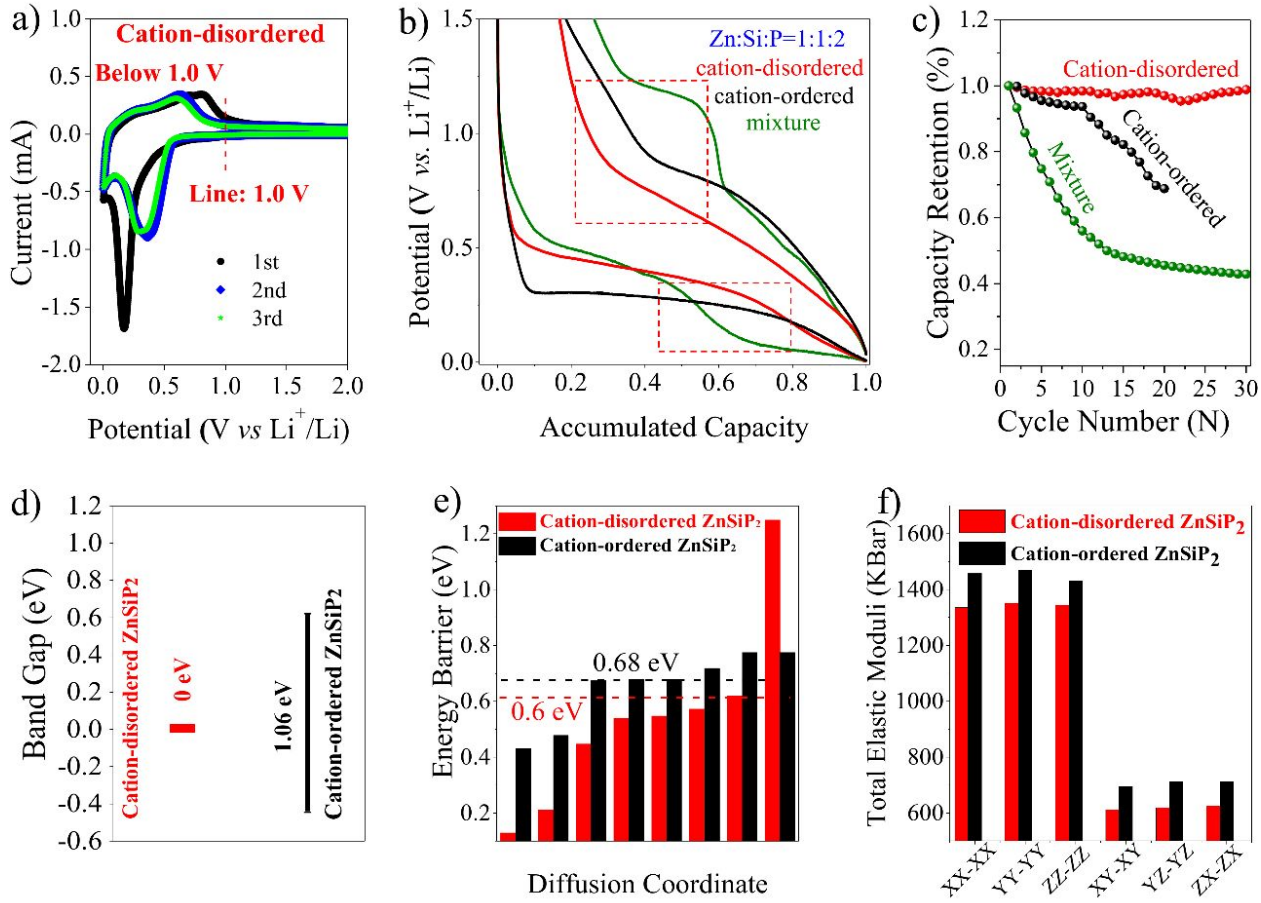

Figure 2. a) The initial three cyclic voltammetry (CV) curves of the cation-disordered $ZnSiP_2$ phase. b) the first-cycle discharge/charge profile comparison; c) the cycle performance comparison of the cation-disordered $ZnSiP_2$ phase, the intermediate product corresponded to the ball milling of 3.0 h and the cation-ordered $ZnSiP_2$ phase also milled at the same experimental condition as the cation-disordered $ZnSiP_2$. d) the band gap comparison; e) the Li-ion activation energy comparison; f) the elastic constant comparison of the cation-disordered $ZnSiP_2$ with the cation-ordered $ZnSiP_2$.

Si. With further increasing milling time to 10 h, there were no significant changes in the XRD pattern. To explore its crystal structure, the related XRD Rietveld refinement is carried out. As shown in **Figure 1b**, all diffraction peaks can be well-indexed by a new cubic phase in the F-43m space group.[40-41] As shown in **Figure 1c**, the refined cell parameters are identical to the ZnS structure counterparts, where Zn and Si atoms randomly occupy the Zn sites (of ZnS) and the P atoms occupy the S sites (of ZnS). The Zn and Si atoms are surrounded in a cubic manner by P atoms and vice versa. Details of the refinement including fractional atomic coordinates, cell parameters are shown in the inset of **Figure 1a**, Table S1 and Table S2. To probe more accurate local information on the crystal structure, we performed transmission electron microscopy (TEM). As shown in the TEM image (Figure S1) and its corresponding selected area electron diffraction (SAED, the inset of Figure S1), the clear ring-like pattern can also be well-assigned to the cubic ZnS crystal structure other than the typical tetragonal cells of the ternary II-IV-V2 semiconductors, because of the lack of diffraction rings corresponding to the extra superstructures. More specifically, this kind of ZnS-like $ZnSiP_2$ phase can also be identified by easy observation of its exposed (110) and (1-10) crystal planes, as indicated by the spacing of lattice fringes in Figure S2. The formation of the cation-disordered $ZnSiP_2$ probably resulted from the high-pressure, high-temperature and natural cooling rate generated by the high energy mechanical ball milling process.[42-43] It is worth noting that the cation-disordered crystal structure has higher symmetry than the corresponding cation-ordered one, which is probably favorable to the long cycle life due to better stress accommodation.[44-45] To compare the electrochemical performance difference of these two phases, we further synthesized the cation-ordered tetragonal phase of $ZnSiP_2$. As shown in **Figure 1d**, the peaks of the cation-ordered $ZnSiP_2$ phase substantially differ from that of the cation-disordered $ZnSiP_2$ due to the appearance of the extra superstructure. The Raman spectroscopy (**Figure 1e**) further demonstrate that the cation-ordered $ZnSiP_2$ phase indeed presents different modes, compared with the cation-disordered $ZnSiP_2$ counterparts, due to the delicate local environmental difference between these two phases (Figure 1c and Figure 1f).

Enlightened by the beneficial compositional and structural characterizations, we anticipated that the cation-disordered $ZnSiP_2$ anode with several Li-reactive components would deliver

attractive Li-storage properties with unique electrochemical behavioural features. **Figure 2a** shows the initial three cyclic voltammetry (CV) curves of the cation-disordered $ZnSiP_2$ anode. During the initial cathodic scan, there is only one reduction band at the beginning of 0.50 V, which is attributed to the Li-ion uptake into the crystal structural lattices of the cation-disordered $ZnSiP_2$. In the subsequent anodic process, there is also only one relative broader shoulder centered at 0.75 V, corresponding to the release of Li-ion from the electrode. It is noted that compared with the initial discharge profile (Figure S3), larger polarization was observed in the initial anodic CV scan, due largely to the relatively faster potential scan rate used for the CV measurements (Figure S4). In the subsequent two cycles, there is almost no change but the reduced polarization benefiting from the activation during the initial lithiation/de-lithiation process. During the initial electrochemical Li-storage process, defects are probably formed in the initial crystal structure, which would assist in the Li-ion transportation during the subsequent cycles.[46-47] In other words, during the initial cycle, the crystal lattice must be relaxed or loosened, therefore it requires less activation energy to transport Li-ion during the subsequent cycles. By careful examination of electrochemical Li-storage behaviours of the cation-disordered $ZnSiP_2$ anodes, there is no hints about the electrochemical Li-storage behavioural features of its single-component P, Si or Zn anodes as compared in Figure S3 and Figure S5 (initial discharge profiles at low current densities of 20 mA g^{-1}, etc.). which implies an intriguing Li-storage mechanism. As shown in Figure S6, the initial discharge of the cation-disordered $ZnSiP_2$ electrode delivers a large capacity of ca. 2000 mA h g^{-1} with only one low and safe working potential plateau of 0.40 V, thus avoiding the dendrite growth like commercially utilized graphite anode caused by the stripping of Li metal as the potential approached zero. During the subsequent charging process, the electrode can still achieve a specific capacity of 1860 mA h g^{-1}, which is five times larger than that of commercial graphite anode. The first-cycle coulombic efficiency is up to 93%. From the second cycle onward (Figure S6), we can see that the reversible discharge/charge capacities can be maintained with little change on discharge/charge profile shapes except for the relative reduced polarization, compared with that of the initial cycle. All the electrochemical Li-storage behaviours exhibited by the galvanostatic discharge/charge profile of the cation-disordered $ZnSiP_2$ accord well with that presented by corresponding CV curves (Figure 2a) during the initial three cycles. To clearly show the unique advantages of the cation-disordered $ZnSiP_2$ anode, the initial discharge/charge features of the cation-disordered $ZnSiP_2$ are compared (**Figure 2b)** with those of the cation-ordered $ZnSiP_2$ (prepared by CVT and then milled under the same conditions used for the cation-disordered $ZnSiP_2$) and an intermediate mixture corresponding to the ball milling time of 3.0 h. The cation-disordered $ZnSiP_2$ anode shows the smallest polarization loss among the three anodes. During the charging process, the cation-disordered $ZnSiP_2$ did not show obvious multi-step reaction plateaus, and also the disappearance of the potential jump from 0.8 to 1.2 V for the cation-disordered $ZnSiP_2$ possibly benefits from its inherent faster reaction kinetics and peculiar Li-storage mechanism to be revealed.[1] As shown in **Figure 2c**, the cycling stability of the cation-disordered $ZnSiP_2$ is also better than that of the intermediate mixture and the cation-ordered electrodes, profiting from its inherent structural advantages.

To track the fundamental reasons behind the electrochemical Li-storage superiority of the cation-disordered $ZnSiP_2$ to the cation-ordered $ZnSiP_2$ counterparts, we utilized the first-principle calculation to provide more insights into the local environment to reveal Li-ion, electron transport properties and resistance to structural variation.[48-52] According to the cation-disordered structural features, we built a random-cation structure shown in Figure S7a.[53] For the electronic structure, to our surprise, as shown in **Figure 2d**, the cation-disordered $ZnSiP_2$ has metallic conductivity featured with no band gap (Figure S7b). However, the cation-ordered $ZnSiP_2$ only shows a semi-conducting feature with a band gap above 1.0 eV based on the simulated electronic structure shown in Figure S7c and Figure S7d, that is consistent with the value reported before.[37] Therefore, we believe that the metallic conductivity of the as-synthesized $ZnSiP_2$ probably benefits from the cation disorder as revealed by various microscopic characterizations. To confirm the enhanced electron transport for the cation-disordered $ZnSiP_2$ predicted by first-principle calculations, we performed electrochemical impedance spectroscopy to determine the charge transfer resistance (R_{ct}) of these electrode materials.[51] As shown in Figure S8, the charge transfer resistance for the cation-disordered $ZnSiP_2$ (~100 Ω) is much smaller than that for the cation-ordered $ZnSiP_2$ (~343 Ω). On the Li-ion storage and transport properties, to optimize the structure with the lowest energy during the simulations at the level of atom, various structural configurations of Li-ion on the lattices and interstitial sites were simulated. The involved lattices were all relaxed at each position by utilizing the primary multiple energy minimization calculation principle. Within the crystal structure of $ZnSiP_2$, there exist four voids, each large enough to host one Li atom. When Li-ion hops among the voids, the activation energy was calculated using the random-cation supercell (Figure S7a). There exist eight Li-ion transportation manners endowed by different local environments brought by the cation disordering within the simulation model. The specific Li-ion diffusion paths following octahedron-tetrahedron-octahedron sites where the site is surrounded by Si or Zn atoms and the corresponding Li-ion activation energy profiles with unsymmetrical features were both presented in Figure S9. As listed in **Figure 2e**, most of the activation energy values are below 0.6 eV. As compared in Figure 2e and Figure S10, however, most activation energies for the cation-ordered $ZnSiP_2$ are above 0.68 eV. These lower migration barriers endowed by the cation-disorder indicates a more facile Li transport in the cation-disordered $ZnSiP_2$ anode. To validate the predictions of theoretical calculations, we used the galvanostatic intermittent titration technique (GITT) to determine Li ion diffusion coefficients in both cation-disordered and cation-ordered $ZnSiP_2$ electrodes.[51] As shown in Figure S11, the average Li-ion diffusion coefficients (especially within the potential window for battery

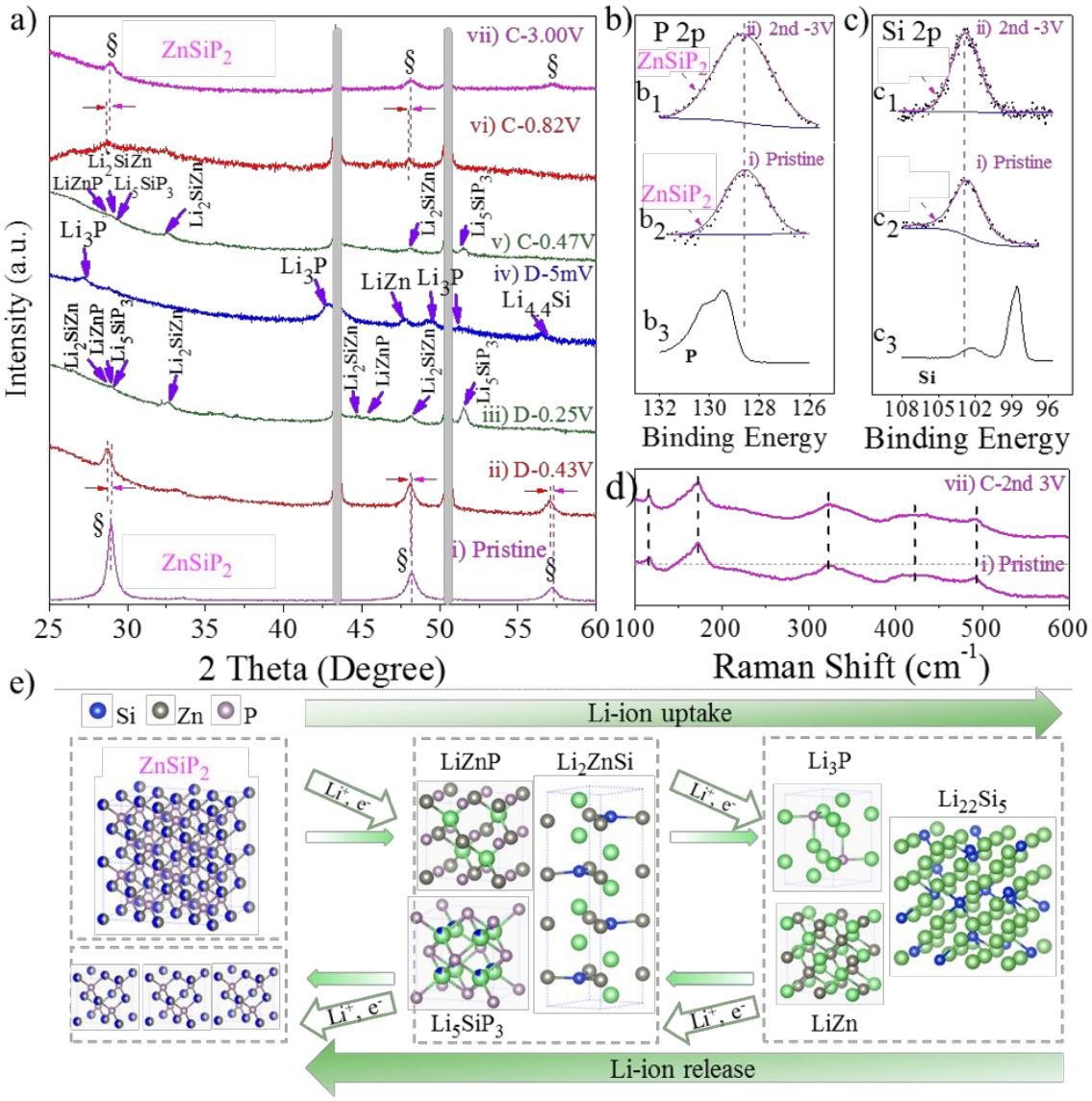

Figure 3. a) the XRD patterns indicative of structural and compositional evolution of the electrode accompanied by lithiation/delithiation process; b) the high-resolution XPS spectra comparison of P 2p of the electrode after the second cycle, the pristine cation-disordered $ZnSiP_2$ and the red P; c) the high-resolution XPS spectra comparison of Si 2p of the electrode after the second cycle with the pristine cation-disordered $ZnSiP_2$ and the raw material Si; d) the Raman spectra comparison of the electrode after the second cycle with the pristine cation-disordered $ZnSiP_2$; e) the illustrated Li-storage mechanism based on the various characterization techniques above.

cycling) of the cation-disordered $ZnSiP_2$ electrode are higher than those of the cation-ordered $ZnSiP_2$ electrode. On the resistance to volume change produced by lithiation/delithiation, we calculated and compared the elastic constants of these two cation-disordered and cation-ordered $ZnSiP_2$ using the first-principle theory.[50-52] As compared in Figure 2f, the cation-disordered $ZnSiP_2$ is softer than the cation-ordered $ZnSiP_2$ since the elastic constants of the cation-disordered $ZnSiP_2$ are smaller than the cation-ordered $ZnSiP_2$ counterparts. The softer property can be mainly attributed to its cation disordering with higher symmetry. Softer property means it is easy to accommodate volume change brought by lithiation/delithiation of the host material.[50-52] To recap, the cation-disordered $ZnSiP_2$ has much faster electronic conductivity (metallic conductivity, **Figure 2d**), much lower activation energy (**Figure 2e**), and better mechanical stability (**Figure 2f**) to structural change than the cation-ordered $ZnSiP_2$ counterparts. The simulation results rationalize the observed superior electrochemical performances of the cation-disordered $ZnSiP_2$ with respect to fast reaction kinetics, small polarization loss, and high energy efficiency compared to the cation-ordered $ZnSiP_2$ counterparts. This demonstrates that the cation-disordered $ZnSiP_2$ would be a high-performance anode material for the next-generation LIBs.

To further elucidate the fundamental reasons behind the electrochemical Li-storage behaviours of the cation-disordered $ZnSiP_2$, structural and compositional evolution of the electrode accompanied by lithiation/delithiation process (Figure S12) was

systematically investigated via XRD, HRTEM along with SAED, XPS and Raman. As shown in **Figure 3a-ii**, with the potential decreased to 0.43 V by discharge, all the fingerprint peaks of cation-disordered $ZnSiP_2$ anode were shifted to the lower 2 theta accompanied with the reduced intensities. This phenomenon can be assigned to the topotactical transformation into Li_xZnSiP_2 (x<2) from the pristine cation-disordered $ZnSiP_2$ with two voids shown in Figure S13. From the corresponding HRTEM and SAED images shown in Figure S14a, the slightly expanded crystal planes of (111), (220) of the cation-disordered $ZnSiP_2$ can be observed. As the discharge proceeds, all the fingerprint peaks of the cation-disordered $ZnSiP_2$ disappeared thoroughly, which is due to the decomposition of Li_2ZnSiP_2 into Li_2ZnSi, Li_5SiP_3 and LiZnP as validated by the subsequent XRD data (**Figure 3a-iii**). The characteristic diffraction peaks of the layered semiconducting Li_2ZnSi (crystal structure shown in Figure S15) at 26.6°, 32.6°, 44.0°, 48.2°, of Li-ion conductor Li_5SiP_3[54] at 26.3°, 51.7°, and of semiconductor LiZnP at 26.8°, 44.5° were observed, respectively. This suggests that the fresh cation-disordered $ZnSiP_2$ anode has been transformed into three phases of Li_2ZnSi, Li_5SiP_3, and LiZnP at the conversion stage, which was confirmed by the corresponding HRTEM and SAED analysis (Figure S14b). When discharged to a terminate potential of 0.005 V (**Figure 3a-iv**), the above-observed ternary lithium-containing phases have disappeared and spontaneously the well-indexed diffractions of Li_3P, $Li_{4.4}Si$ and LiZn alloys appeared, presenting the formation of final lithiation products. The formation of the final binary lithiated products can also be supported by the corresponding HRTEM images and SAED patterns as shown in Figure S14c. Based on these results, the cation-disordered $ZnSiP_2$ electrode can deliver ca. 2000 mA h g^{-1}, also coinciding with the discharge capacity. In the subsequent charge process, the XRD fingerprint signals of these binary lithium-containing Li_3P, $Li_{4.4}Si$ and LiZn alloyed phases were dramatically weakened or disappeared with the reappearance of the fingerprint signals of the Li_2ZnSi, Li_5SiP_3, and LiZnP phases. However, when the potential was increased to 0.47 V by charge, the characteristic peaks of the re-formed Li_2ZnSi, Li_5SiP_3, and LiZnP phases were very weak due to the lost crystallinity during cycling **(Figure 3a-v** and Figure S14d). All the charged observations were also well consistent with the corresponding HRTEM images and SAED patterns as shown in Figure S14e. This is presumably because these electrochemical reaction products at this stage are in low crystallinity due to more Li-extraction during the charge and well-distributed in the carbon matrix, thus rendering their X-ray signals almost invisible as shown in **Figure 3a-vi**. When completely charged back to 3.0 V, the fingerprint peaks of the cation-disordered $ZnSiP_2$ phase have been reformed, as shown in **Figure 3a-vii** and Figure S14f. In addition, the ex-situ XPS (**Figure 3b-Figure 3c**) and Raman (**Figure 3d**) results of the second cycle definitely showed the reappearance of the cation-disordered $ZnSiP_2$, demonstrating that the cation-disordered $ZnSiP_2$ was recombined during the final charge step. It could also be supported by the similarity of the discharge/charge behaviours of the subsequent cycles to the initial one (Figure S6) while very different from that of the corresponding single-component anodes shown in Figure S3. Moreover, after 30 cycles, the recombination can still be validated based on various characterization techniques as shown in Figure S16-S18. This recombination phenomenon was quite interesting and similar to that observed within the nanosized transition-metal oxides and chalcogenides, like Li_2TiSiO_5, Fe_2CoSe_4.[55-56] On the basis of the XRD along with HRTEM, XPS, Raman results and the electrochemical Li-storage behaviours of the cation-disordered $ZnSiP_2$, a reaction mechanism (**Figure 3e**) was proposed and summarized as follows:

during the discharge process,

the initial stage (intercalation)

$ZnSiP_2 + xLi^+ + xe^- \rightarrow Li_xZnSiP_2$ (intercalation, $x \leqq 2$) (1);

the second stage (conversion)

$2Li_2ZnSiP_2 + 4Li^+ + 4e^- \rightarrow Li_2ZnSi + Li_5SiP_3 + LiZnP$ (2);

the third stage (re-conversion)

$Li_2ZnSi+Li_5SiP_3+LiZnP+14.8Li^+ + 14.8e^- \rightarrow 2Li_{4.4}Si+2LiZn+4Li_3P$ (3);

During the charge process,

the initial stage (de-reconversion)

$2Li_{4.4}Si + 2LiZn + 4Li_3P\text{-}14.8Li^+\text{-}14.8e^- \rightarrow Li_2ZnSi+Li_5SiP_3+LiZnP$ (4);

the second stage (de-conversion)

$Li_2ZnSi + Li_5SiP_3 + LiZnP - 4Li^+ - 4e^- \rightarrow 2\ Li_2ZnSiP_2$ (5);

The third stage (de-intercalation)

$Li_2ZnSiP_2 - xLi^+ - xe^- \rightarrow Li_{2-x}ZnSiP_2$ ($x \leqq 2$). (6).

In total: $ZnSiP_2 + 11.4Li^+ + 11.4e^- \leftrightharpoons 2Li_3P + Li_{4.4}Si + LiZn$ (7).

In short, during discharge, the $ZnSiP_2$ electrode underwent electrochemical reactions comprised of intercalation, conversion, and re-conversion in sequence. During the charge process, all these corresponding reaction sequences appeared to be reversible, until reformation of the initial crystal structure of the cation-disordered $ZnSiP_2$. Based on this peculiar Li-storage mechanism, the cation-disordered $ZnSiP_2$ electrode could accommodate 11.4 Li-ions per formula, corresponding to 1,970 mA h g^{-1}, where the two P atoms contribute 1,037 mA h g^{-1}, the one Si atom contributes 760 mA h g^{-1}, and the Zn atom donates the remaining 173 mA h g^{-1}. As estimated from the discharge/charge tests, the first discharge capacity for the cation-disordered $ZnSiP_2$ is ca. 2,000 mA h g^{-1}, approaching the theoretical value, which implies the complete conversion reaction of $ZnSiP_2$ for Li-storage is as depicted in **Equation 7**.

To further prolong the cycle life and boost the rate performance of cation-disordered $ZnSiP_2$ electrode, the material was mixed with commercial graphite via the facile mechanical ball milling method. The XRD diffraction peaks of the resulting $ZnSiP_2$/C composite (Figure S19) can be well-indexed although with a slight reduced peak intensity and broader half-width, implying that the milled process produces enough energy to break the layered graphite to encapsulate the well-distributed $ZnSiP_2$. Furthermore, the as-milled graphite composite is composed of numerous nanosized irregular shaped particles that is well-populated within the carbon matrix (Figure S20), which agglomerate into larger microsized secondary particles with little BET surface area of 12.4 $m^2\ g^{-1}$

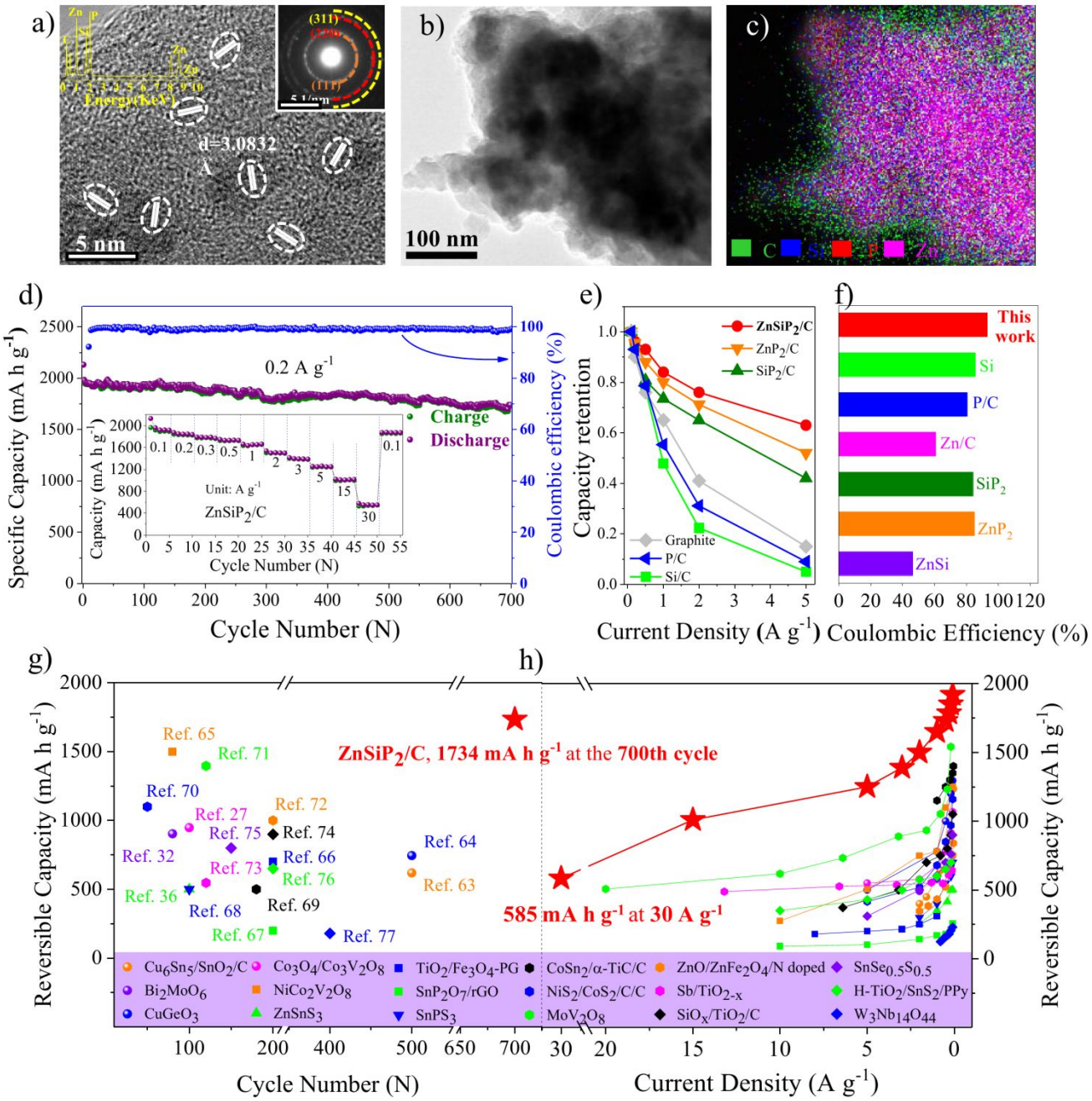

Figure 4. a) the high-resolution TEM image (HRTEM) of the cation-disordered $ZnSiP_2$/graphite composite; b) the TEM frame image used for elemental mapping of the cation-disordered $ZnSiP_2$/graphite composite; c) the elemental mapping of the cation-disordered $ZnSiP_2$/graphite composite; d) the long-cycle stability of the cation-disordered $ZnSiP_2$/graphite composite and the inset is the rate performance; e) the rate performance comparison of the cation-disordered $ZnSiP_2$/graphite composite with the related binary phase graphite and single-component graphite composites prepared in our lab at the same experimental conditions; f) the first-cycle Coulombic efficiency comparison of the cation-disordered $ZnSiP_2$/graphite composite with the related binary-component graphite and single-component graphite composites prepared in our lab at the same experimental conditions. The performance comparison of the cation-disordered $ZnSiP_2$/C with multi-phase anodes studied: g) the cycle stability comparison at relative small current densities; h) the rate performance comparison.

(Figure S21). The featured morphology of $ZnSiP_2$/C inherently favors for the Li-storage in the following two aspects. First, the nanoparticles would facilitate the electrolyte permeation along the numerous grain boundaries, where Li-ion transfer capability is also much faster than that within the crystals, shorten the Li-ion diffusion length, and decrease structural strain, compared with large-size single crystals and bulk samples prepared via solid-state calcination. Second, the large aggregated microsized particles would favor the formation of stable SEI film at the

electrode/electrolyte interfaces, which could improve the initial coulombic efficiency by decreasing the side reactions brought by nano and also help increase the tap density to promote energy density, compared with overlarge BET electrode materials. As seen from the HRTEM image of $ZnSiP_2$/C nanocomposite, the nanosized crystalline domains of $ZnSiP_2$ (<5 nm) were well-embedded into the amorphous carbon matrix and distributed evenly. As shown in **Figure 4a**, the periodical lattice fringes with a d-spacing of 0.308 nm could be assigned to the (111) crystal plane of crystalline $ZnSiP_2$ particle. From the SAED pattern (the inset of Figure 4a), we can see the halo-like multiple rings with some well-dispersed spots, which indicates that a large number of $ZnSiP_2$ nanoparticles were well-distributed in the amorphous carbon matrix. The TEM-based energy dispersive X-ray spectroscopy (EDX, the inset of **Figure 4a**) demonstrates the atomic ratio of Zn, Si and P is approximately 1:1:2. As shown in **Figure 4b**, **4c**, the color-coded element mappings show the homogeneous distribution of Zn, Si, P and C throughout the nanocomposite, indicating that $ZnSiP_2$ are composited with graphite to form an ultrafine nanocomposite thanks to the presence of graphite, which alleviates the aggregation issue during the mechanical milling. The well-hybridized nanocomposite accelerates e^-, Li^+ transfer and accommodate large volume change throughout the whole electrochemical Li-storage process. As shown in **Figure 4d**, $ZnSiP_2$/C delivered considerable cycling stability with the remaining capacity of 1789 mA h g^{-1} after 700 cycles at a current density of 200 mA g^{-1} at a potential range of 3.0-0.005 V. More impressively, as shown in Figure S22, at a high current density of 2 A g^{-1}, the $ZnSiP_2$/C electrode still retained 1278 mA h g^{-1} after 2,000 cycles, accounting for 84.6 % of the initial reversible capacity. Also, the coulombic efficiency vs. cycle number plot reached 99.5% except for the initial cycle, which further indicated that the $ZnSiP_2$/C anode obtained inherent high reversibility for Li-storage. Moreover, $ZnSiP_2$/C shows excellent reversible capacity retention at different current densities (**the inset of Figure 4d**). High reversible capacities of 1920 mA h g^{-1} at 0.1 A g^{-1}, 1850 mA h g^{-1} at 0.2 A g^{-1}, 1785 mA h g^{-1} at 0.3 A g^{-1}, 1730 mA h g^{-1} at 0.5 A g^{-1}, 1650 mA h g^{-1} at 1.0 A g^{-1}, 1500 mA h g^{-1} at 2.0 A g^{-1}, 1390 mA h g^{-1} at 3.0 A g^{-1}, 1250 mA h g^{-1} at 5.0 A g^{-1}, and 1010 mA h g^{-1} at 15.0 A g^{-1} could be achieved, thus showing the ultrahigh-rate capability of the $ZnSiP_2$/C electrode. Even at an ultrahigh current density of 30 A g^{-1}, the reversible specific capacity could reach as high as 585 mA h g^{-1}, which is still larger than the theoretical capacity of graphite (372 mA h g^{-1}). Furthermore, 98% of its first-cycle reversible capacity could be attained, when the current density was decreased back to 0.1 A g^{-1}. As compared in **Figure 4e**, **4f**, the cation-disordered $ZnSiP_2$/C anodes deliver the best performances in terms of the rate performance and first-cycle coulombic efficiencies among its related binary- or single-component anode counterparts. Moreover, as compared in **Figure 4g, 4h**, the cycle stability and rate performance of the cation-disordered $ZnSiP_2$/C anode surpasses all the multi-phase anodes studied.[27,32,36,63-77] The superiority mainly benefitted from the inherent merits of the cation-disordered $ZnSiP_2$ like metallic conductivity, the introduced graphite carbon as a buffer matrix to accommodate the volume change during cycling and the ternary mediate electrochemical products like Li_2ZnSi, Li_5SiP_3 and LiZnP, which also obtained inherent fast Li-ion and electron transfer capability.

Considering the versatility of the cation-disorder, we further expand the horizon to include a novel family of Zn(Cu)-Si-P based on the specific cation-disordered $ZnSiP_2$ case and evaluate their Li-storage performances. Firstly, considering the cation-disordered feature of the as-synthesized $ZnSiP_2$, the materials with different Zn/Si ratios were synthesized. As shown in **Figure 5a**, with increasing molar ratio of Si within the cation sites of the Zn-Si-P, all the Si-like peaks ($ZnSi_2P_3$ → $ZnSi_3P_4$ → $ZnSi_4P_5$) shift to the higher angles (**Figure 5b**), which indicates they have similar crystal structure, but with some shrinkage due to smaller atomic size of Si compared to Zn. Secondly, as known, Cu is located next to Zn in the Periodic Table and moreover, as a non-competitive element with the cathode it is widely used in our daily life because of its excellent conductivity. Considering these facts and its similar atomic sizes, bonding characteristics and electronegativity to that of Zn, we further replace Zn with Cu to further extend the family and meanwhile change the cation Cu/Si ratios. As expected, the Cu-Si-P ($CuSi_2P_3$ → $CuSi_3P_4$ → $CuSi_4P_5$) show similar structural characteristics (**Figure 5c-Figure 5d**) to that of the Zn-Si-P compounds. Actually, Zn(Cu)-Si-P atoms can be exchanged with each other in a large range as discussed above. All these results indicate that these cation-disordered atomic arrangements seem to involve the similar atoms in a wide range. As known, the physicochemical properties including electrochemical performances of the materials depend on the crystal structure and components and meanwhile can be largely affected by the doping.[57-58] Therefore, we investigate and compare the electrochemical Li-storage behaviours of the above synthesized cation-disordered family (Zn(Cu)-Si-P). As compared in **Figure 5e**, **5f**, all these cation-disordered anodes can deliver large discharge capacities within the range of 1900-2600 mA h g^{-1} (**insets of Figure 5e**), which approaches the theoretical capacity based on the corresponding binary Li-alloy products ($Li_{4.4}Si$, LiZn and Li_3P), with very high initial coulombic efficiency above 90% (**insets of Figure 5e**). More importantly, all of them deliver an appropriate low and safe working potential within the range of 0.4-0.5 V vs. Li^+/Li (**Figure 5f**). The working potential is above the lithium plating potential like that of silicon and graphite, which avoids the formation of dendrite to impale the separator especially at high-rate. The working potential of the new anode family is not as high as that of phosphorus, which could achieve competitive energy density applied in full cells. Accordingly, we develop a novel family of cation-disordered anode materials with more practical work potential filling the gap between that of silicon and P/C composite, thus meeting the demands of both high safety and high energy density when applied in full cells.

In summary, we synthesized a new cation-disordered $ZnSiP_2$ by a facile ball milling method. When used as an anode for LIBs, the cation-disordered $ZnSiP_2$ anode delivers enhanced Li-storage properties compared to that of the cation-ordered $ZnSiP_2$ in term of reaction kinetics and energy efficiency. The

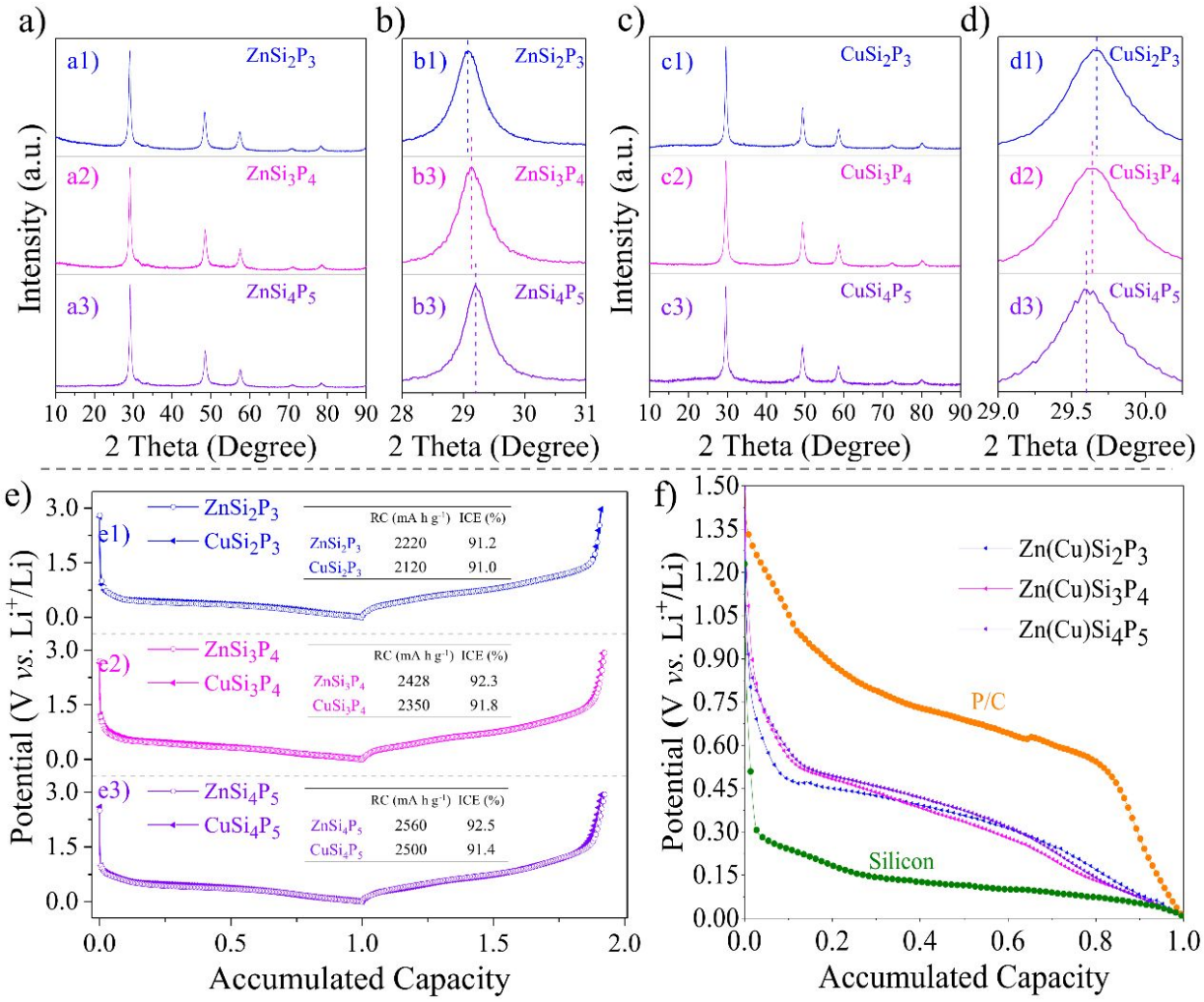

Figure 5. a) the XRD patterns of the ternary cation-disordered Zn-Si-P compounds ($ZnSi_2P_3$ → $ZnSi_3P_4$ → $ZnSi_4P_5$); b) the enlarged XRD patterns of the first strongest peak to identify the shift of peak position. c) the XRD patterns of the ternary cation-disordered Cu-Si-P compounds ($CuSi_2P_3$ → $CuSi_3P_4$ → $CuSi_4P_5$); d) the enlarged XRD patterns of the first strongest peak to identify the shift of peak position. e) the initial discharge/charge profile comparison of the ternary cation-disordered Zn-Si-P with Cu-Si-P compounds; f) the typical discharge profile comparison of the above Zn(Cu)-Si-P family with P/C and Si anodes. Note that "RC" means reversible capacity and "ICE" means initial coulombic efficiency.

superiority is attributed to the faster transport of e^- and Li^+ as well as the better endurance to volume variation of the cation-disordered $ZnSiP_2$ than the cation-ordered $ZnSiP_2$ counterparts, as confirmed by first-principle calculations and electrochemical impedance spectroscopy. The cation-disordered cubic $ZnSiP_2$ undergoes intercalation, conversion, and re-conversion reactions. During the de-lithiation process, all the lithiation reactions are reversed, including the structural evolution, until the original crystal structure is re-constructed, as confirmed by XRD along with HRTEM, Raman, XPS, and electrochemical measurements. The carbon composite ($ZnSiP_2$/C) achieves long-term cyclability (a reversible capacity of 1278 mA h g^{-1} after 2,000 cycles at a current density of 2000 mA g^{-1}, accounting for 84.6 % of the initial reversible capacity) and high-rate performance (585 mA h g^{-1} at 30 A g^{-1}). The cycle and rate performance surpass all the reported multi-phase anodes studied. These superior performances also benefit from the synergetic Li-storage capability of each component and the intermediate electrochemical products like Li_2ZnSi, Li_5SiP_3 and LiZnP, which have excellent electron and Li-ion transfer capability. Furthermore, the introduced graphite provides not only a continuous network for efficient current collection but also a structural framework for accommodation of the volume changes during Li-ion insertion/retraction. The concept of the cation-disordered $ZnSiP_2$ can be further extended to a family of cation-disordered Zn(Cu)-Si-P materials with a wide range of cation ratios, which has never before been synthesized. All these materials show large capacity, high initial Coulombic efficiency, and proper working potentials between those for P/C and Si anodes.

Experimental Section

Material preparation

All these cation-disordered Zn(Cu)-Si-P (including $ZnSiP_2$, $ZnSi_2P_3$, $ZnSi_3P_4$, $ZnSi_4P_5$, $CuSi_2P_3$, $CuSi_3P_4$, and $CuSi_4P_5$) samples were prepared by a low-cost and scalable mechanical ball milling method by sealed element powders in a given ratio into a vessel with the protection gas of argon. To obtain a high impact energy, the selected grinding bowl with volume of 500 mL and grinding balls in diameter of 10 mm are both stainless steel. The grinding balls and the mixture of Zn(Cu), Si and red P (3 g) were placed in the in the grinding bowl in sequence. The materials to steel balls mass ratio is 1:25. When ground by the planetary mono mill (Fritsch Pulverisette-6) at a speed of 300 rpm, the milling duration is 10 min and rests for 5 min. To obtain better mechanical alloying, the reversing operation mode (regular reversal of the direction of rotation) is adopted. The cation-ordered $ZnSiP_2$ was synthesized by the CVT reported before.[42-43] When served for anodes, it was ball milled at the same experimental conditions as that of the cation-disordered $ZnSiP_2$. The $ZnSiP_2$/C, the related single-component carbon composites (P/C, Si/C, Zn/C), and the related binary-component carbon composites (ZnP_2/C, ZnSi/C, SiP_2/C) were also synthesized by further milled the as-prepared compounds with the commercial graphite in a mass ratio of 7:2 for the duration of 2.0 h at the similar experimental conditions.

Material characterization

All these samples were performed by the X-ray diffraction (PANalytical X'pert PRO-DY2198 with Cu-Kα radiation). The related morphology was observed by field-emission scanning electron microscope (FSEM, FEI Quanta650), and the micro-structures were detected by the transmission electron microscope (TEM, JEOL JEM 2100) including high resolution transmission electron microscope (HRTEM) and the selected area electron diffraction (SAED). The related valence and composition analysis were carried out via the X-ray photoelectron spectroscopy (Thermo Fisher ESCALab250 with the monochromatic 150 W AlKα radiation). The related Raman data were collected by confocal Raman spectrometer (Raman, WTEC ALPHA300 with the 532 nm excitation laser).

Electrochemical characterization

For pure phase, all these active materials were milled with carbon black and Li-PAA in mass ratio of 7:2:1. The slurries were pasted onto a copper foil and dried under vacuum at 100 °C for 24 h. For the related carbon composites, these composites were directly milled with Li-PAA in 9:1 (mass ratio). The loading materials were 1.8-2 mg cm^{-2}. The diameter of the electrode is 8 mm. The electrochemical characterizations were conducted utilizing coin-type cells (CR2032) sealed in the glovebox (Mbraun, Labmaster 130) full of argon, where the contents of O_2 and H_2O were both controlled under 0.01 ppm. Li foils were served as counter and reference electrodes, and the related electrolytes were 1 M $LiPF_6$ dissolved in EC/DEC (1:1 by volume). The Li-storage discharge/charge tests were conducted on a LAND battery tester (Wuhan Kingnuo Electronic Co., China) and on the testing system (Hokuto Denko, HJ1001SD8). The cyclic voltammetric (CVs) measurements were conducted on the electrochemical workstation (Autolab, Pgstat 302N). As for an Accumulated Capacity, the test conditions are as usual: the cycling rate was 200 mA g^{-1} in the potential range of 3.0-0.005 V. In order to compare the electrochemical behaviors, both the discharge and charge capacity were normalized by the initial discharge capacity.

Calculations detail

First-principles calculations was carried out using VASP (Vienna Ab-initio Simulation Package).[59] The exchange-correlation functional with generalized gradient approximation parameterized by Perdew, Burke and Ernzerhof was used.[60] The core-electrons were kept frozen in the form of projector augmented wavefunction,[61] with valence electron configuration for P $3s^23p^3$, Si $3s^23p^2$, Zn $3d^{10}4s^2$. The 4x4x4 Monkhorst-Pack reciprocal grid, together with 400 eV energy cutoff was used for sufficient energy calculations.[62] Gaussian smearing with smearing width of 0.05 eV was used to accelerate computation of electronic energy near Fermi level.

Acknowledgements

This work was supported by the National Natural Science Foundation of China (21701030, 51801096), Guangdong Province Natural Science Foundation (2017A030310241), Innovative talents cultivation project of outstanding youth in Guangdong Province (2016KQNCX038), Science and Technology Planning Project of Guangzhou City (201804010392), China Postdoctoral Science Foundation funded project (No. 1112000139), Guangdong Innovative and Entrepreneurial Research Team Program (No. 2014ZT05N200), and US National Science Foundation (DMR-1742828). The authors acknowledge the use of facilities in Guangdong University of Technology, Georgia Institute of Technology, and Southern University of Science and Technology. Computational work used resources of the National Energy Research Scientific Computing Center (NERSC), a U.S. Department of Energy Office of Science User Facility operated under Contract No. DE-AC02-05CH11231.

References

1 Y. Wei, L. Huang, J. He, Y. Guo, R. Qin, H. Li and T. Zhai, *Adv. Energy Mater.*, 2018, **8**, 1703635.

2 Q. Xu, J. Li, J. Sun, Y. Yin, L. Wan and Y. Guo, *Adv. Energy Mater.*, 2017, **7**, 1601481.

3 W. Li, Y. Yang, G. Zhang and Y. Zhang, *Nano Lett.*, 2015, **15**, 1691-1697.

4 W. Chang, K. Tseng and H. Tuan, *Nano Lett.*, 2017, **17**, 1240-1247.

5 J. Zhou, X. Liu, W. Cai, Y. Zhu, J. Liang, K. Zhang, Y. Lan, Z. Jiang, G. Wang and Y. Qian, *Adv. Mater.*, 2017, **29**, 1700214.

6 Q. Xiao, Q. Zhang, Y. Fan, X. Wang and R. A. Susantyoko, *Energy Environ. Sci.*, 2014, **7**, 2261-2268.

7 J. Lee, Y. Ko, M. Shin, H. Song, N. Choi, M. Kim and S. Park, *Energy Environ. Sci.*, 2015, **8**, 2075-2084.

8 X. Li, P. Yan, X. Xiao, J. Woo, C. Wang, J. Liu and J. Zhang, *Energy Environ. Sci.*, 2017, **10**, 1427-1434.
9 J. H. Lee, C. S. Yoon, J. Y. Hwang, S. J. Kim., F. Maglia, P. Lamp, S. T. Myung and Y. K. Sun, *Energy Environ. Sci.*, 2016, **9**, 2152-2158.
10 S. Chae, M. Ko, S. Park, N. Kim, J. Ma and J. Cho, *Energy Environ. Sci.*, 2016, **9**, 1251-1257.
11 N. Lin, Y. Han, J. Zhou, K. Zhang, T. Xu, Y. Zhu and Y. Qian, *Energy Environ. Sci*., 2015, **8**, 3187-3191.
12 Y. Jin, S. Li, A. Kushima, X. Zheng, Y. Sun, J. Xie, J. Sun, W. Xue, G. Zhou, J. Wu, F. Shi, R. Zhang, Z. Zhu, K. So, Y. Cui and J. Li, *Energy Environ. Sci.*, 2017, **10**, 580-592.
13 D. Lin, Z. Lu, P. Hsu, H. R. Lee, N. Liu, J. Zhao, H. Wang, C. Liu and Yi Cui, *Energy Environ. Sci.*, 2015, **8**, 2371-2376.
14 Q. Zhang, H. Chen, L. Luo, B. Zhao, H. Luo, X. Han, J. Wang, C. Wang, Y. Yang, T. Zhu and M. Liu, *Energy Environ. Sci.*, 2017, **10**, 580-592.
15 C. Du, C. Gao, G. Yin, M. Chen and L. Wang, *Energy Environ. Sci.*, 2011, **4**, 1037-1042.
16 S. Liu, J. Feng, X. Bian, J. Liu, H. Xu and Y. An, *Energy Environ. Sci.*, 2017, **10**, 1222-1233.
17 W. Zhang, J. Mao, S. Li, Z. Chen and Z. Guo, *J. Am. Chem. Soc.*, 2017, **139**, 3316-3319.
18 L. Chen, G. Zhou, Z. Liu, X. Ma, J. Chen, Z. Zhang, X. Ma, F. Li, H. Cheng and W. Ren, *Adv. Mater.*, 2016, **28**, 510-517.
19 Z. Huang, H. Hou, Y. Zhang, C. Wang, X. Qiu and X. Ji, *Adv. Mater.*, 2017, **29**, 1702372.
20 W. Li, S. Hu, X. Luo, Z. Li, X. Sun, M. Li, F. Liu and Y. Yu, *Adv. Mater.*, 2017, **29**, 1605820.
21 J. Liu, P. Kopold, C. Wu, P. A. Van Aken, J, Maier and Y. Yu, Energy Environ. Sci., 2015, **8**, 3531-3538.
22 S. Liu, J. Feng, X. Bian, J. Liu, H. Xu and Y. An, *Energy Environ. Sci.*, 2017, **10**, 1222-1233.
23 Y. Liu, A. Zhang, C. Shen, Q. Liu, X. Cao, Y. Ma, L. Chen, C. Lau, T. Chen, F. Wei and C. Zhou, *ACS Nano*, 2017, **11**, 5530-5537.
24 J. Ni, L. Li and J. Lu, *ACS Energy Lett.*, 2018, **3**, 1137-1144.
25 R. Hu, Y. Ouyang, T. Liang, H. Wang, J. Liu, J. Chen, C. Yang, L. Yang and M. Zhu, *Adv. Mater.*, 2017, **29**,1605006.
26 W. Zhang, J. Mao, W. Pang, Z. Guo and Z. Chen, Electrochim. Acta., 2017, **235**, 107-113.
27 Y. Lu, L. Yu, M. Wu, Y. Wang and X. Lou, *Adv. Mater.*, 2018, **30**, 1702875.
28 D. Pham-Cong, J. Choi, J. Yun, A. Bandarenka, J. Kim, P. Braun, S. Jeong and C. Cho, *ACS Nano.*, 2017, **11**,1026-1033.
29 C. Chen, X. Xie, B. Anasori, A. Sarycheva, T. Makaryan, M. Zhao, P. Urbankowski, L. Miao, J. Jiang and Y. Gogotsi, *Angew. Chem.*, 2018, **57**,1846-1850.
30 S. Cao, Z. Xue, C. Yang, J. Qin, L. Zhang, P. Yu, S. Wang, Y. Zhao, X. Zhang and R. Liu, *Nano energy,* 2018, **50**, 25-34.
31 P. Wu, A. Zhang, L. Peng, F. Zhao, Y. Tang, Y. Zhou and G. Yu, *ACS Nano*, 2018, **12**, 759-767.
32 Y. Zheng, T. Zhou, X. Zhao, W. Pang, H. Gao, S. Li, Z. Zhou, H. Liu and Z. Guo, *Adv. Mater.*, 2017, **29**, 1700396.
33 K. J. Griffith, K. M. Wiaderek, G. Cibin, L. E. Marbella and C. P. Grey, *Nature*, 2018, **559**, 556-563.
34 X. Wang, D. Chen, Z. Yang, X. Zhang, C. Wang, J. Chen, X. Zhang and M. Xue, *Adv. Mater.*, 2016, **28**, 8645-50.
35 Z. li, M. Asif, X. Huang, T. Tang and Y. Hou, Adv. Mater., 2018, **30**, 1802745.
A. AbdelHamid, J. Soh, Y. Yu and J. Ying, *Nano Energy*, 2018, **44**, 399-410.
36 X. Liu, Y. Hao, J. Shu, H. Sari, L. Lin, H. Kou, J. Li, W. Liu, B. Yan, D. Li, J. Zhang and X. Li, *Nano Energy*, 2019, **57**, 414-423.
37 A. D. Martinez, A. N. Fioretti, E. S. Toberer and A. C. Tamboli, *J. Mater. Chem. A*, 2017, **5**, 11418-11435.
38 A. D. Martinez, E. L. Warren, P. Gorai, K. A. Borup, D. Kuciauskas, P. C. Dippo, B. R. Ortiz, R. T. Macaluso, S. D. Nguyen, A. L. Greenaway, S. W. Boettcher, A. G. Norman, V. Stevanović, E. S. Toberer and A. C. Tamboli, *Energy Environ. Sci.*, 2016, **9**, 1031-1041.
39 A. D. Martinez, E. M. Miller, A. G. Norman, R. R. Schnep, N. Leick, C. Perkins, P. Stradins, E. S. Toberer and A. C. Tamboli, *J. Mater. Chem. C*, 2018, **6**, 2696-2703.
40 Bennacer and Hamza, *Appl. Phys. Lett.*, 2017, **110**, 182106.
41 S. Nakatsuka and Y. Nose, *J. Phys. Chem. C*, 2017, **121**, 1040-1046.
42 D. O. Scanlon and A. Walsh, *Appl. Phys. Lett.*, 2012, **100**, 251911.
43 M. A. Ryan, M. W. Peterson, D. L. Williamson, J. S. Frey, G. E. Maciel and B. A. Parkinson, *J. Mater. Res.*, 1987, **2**, 528-537.
44 H. H. Heenen, C. Scheurer and K. Reuter, *Nano Lett.*, 2017, **17**, 3884-3888.
45 J. Sun, H. Lee, M. Pasta, H. Yuan, G. Zheng, Y. Sun, Y. Li and Y. Cui, *Nat. Nanotech.,* 2015, **10**, 980-985.
46 K. Zhang, M. Park, L. Zhou, G. Lee, W. Li, Y. Kang and J. Chen, *Adv. Funct. Mater.*, 2016, **26**, 6728-6735.
47 K. Zhang, M. Park, L. Zhou, G. Lee, J. Shin, Z. Hu, S. Chou, J. Chen and Y. Kang, *Angew. Chem.*, 2016, **55**, 12822-12826.
48 M. S. Islam and G. A. J. Fisher, Chem. *Soc. Rev.*, 2014, **43**, 185-204.
49 Q. Bai, L. Yang, H. Chen and Y. Mo, *Adv. Energy Mater.*, 2018, **8**, 1702998.
50 K. Duho, K. Zhang, J. Lim, G. Lee, K. Cho, M. Cho and Y. Kang, Mater. *Today Energy*, 2018, **9**, 126-136.
51 D. Kim, K. Zhang, M. Cho and Y.-M. Kang, *Energy Environ. Sci.*, 2019, **10**.1039/C9EE00283A.
52 K. Zhang, D. Kim, Z. Hu, M. Park, G. Noh, Y. Yang, J. Zhang, V. W.-h. Lau, S.-L. Chou, M. Cho, S.-Y. Choi and Y.-M. Kang, *Nat. Commun.*, 2019, **10**, 5203.
53 A. Zunger, S. Wei, L. Ferreira and J. E. Bernard, *Phys. Rev. Lett.*, 1990, **65**, 353-356.
54 M. S. A. Haffner, T. Bräuniger and D. Johrendt, *Angew. Chem.*, 2016, **55**,13585-13588.
55 J. Liu, W. Pang, T. Zhou, L. Chen, Y. Wang, V. K. Peterson, Z. Yang, Z. Guo and Y. Xia, *Energy Environ. Sci.*, 2017, **10**, 1456-1464.
56 Z. Ali, M. Asif, X. Huang, T. Tang and Y. Hou, *Adv. Mater.*, 2018, **30**, 1802745.
57 C. Yan, G. Chen, X. Zhou, J. Sun and C. Lv, *Adv. Funct. Mater.*, 2016, **26**, 1428-1436.

58 B. Hou, Y. Wang, D. Liu, Z. Gu, X. Feng, H. Fan, T. Zhang, C. Lü and X. Wu. *Adv. Funct. Mater.*, 2018, **28**,1805444.

59 G. Kresse and J. Furthmüller, *Phys. Rev. B*, 1996, **54**, 11169-11186.

60 J. P. Perdew, K. Burke and M. Ernzerhof, *Phys. Rev. Lett.*, 1996, **77**, 3865-3868.

61 G. Kresse, *Phys. Rev. B*, 1999, **59**, 1758-1775.

62 J. D. Pack and H. J. Monkhorst, *Phys. Rev. B,* 1977, **16**, 1748-1749.

63 R. Hu, G. H. Waller, Y. Wang, Y. Chen, C. Yang, W. Zhou, M. Zhu and M. Liu, *Nano Energy*, 2015, **18**, 232-244.

64 Y. Liu, T. Zhou, Y. Zheng, Z. He, C. Xiao, W. K. Pang, W. Tong, Y. Zou, B. Pan, Z. Guo and Y. Xie, *ACS Nano*, 2017, **11**, 8519-8526.

65 Y. Lu, J. Nai and X. W. D. Lou, *Angew. Chem.,* 2018, **57**, 2899-2903.

66 L. Pan, X.-D. Zhu, X.-M. Xie and Y.-T. Liu, *Adv. Funct. Mater.*, 2015, **25**, 3341-3350.

67 J. Pan, S. Chen, D. Zhang, X. Xu, Y. Sun, F. Tian, P. Gao and J. Yang, *Adv. Funct. Mater.*, 2018, **28**, 1804672.

68 E. Edison, A. Chaturvedi, H. Ren, S. Sreejith, C. T. Lim and S. Madhavi, *ACS Appl. Energy Mater.*, 2018, **1**, 5772-5778.

69 M.-G. Park, D.-H. Lee, H. Jung, J.-H. Choi and C.-M. Park, *ACS Nano*, 2018, **12**, 2955-2967.

70 Y. Lin, Z. Qiu, D. Li, S. Ullah, H. Yang, H. Xin, W. Liao, B. Yang, H. Fan, J. Xu and C. Zhu, *Energy Storage Mater.*, 2018, **11**, 67-74.

71 H. Zheng, Q. Zhang, H. Gao, W. Sun, H. Zhao, C. Feng, J. Mao and Z. Guo, *Energy Storage Mater.*, 2019, DOI: 10.1016/j.ensm.2019.01.005

72 Y. Ma, Y. Ma, D. Geiger, U. Kaiser, H. Zhang, G.-T. Kim, T. Diemant, R. J. Behm and A. Varzi, S. Passerini, *Nano Energy*, 2017, **42**, 341-352.

73 N. Wang, Z. Bai, Y. Qian and J. Yang, *Adv. Mater.*, 2016, **28**, 4126-4133.

74 Z. Li, H. Zhao, P. Lv, Z. Zhang, Y. Zhang, Z. Du, Y. Teng, L. Zhao and Z. Zhu, *Adv. Funct. Mater.*, 2018, **28**, 1605711.

75 Q. Tang, Y. Cui, J. Wu, D. Qu, A. P. Baker, Y. Ma, X. Song and Y. Liu, Nano Energy, 2017, **41**, 377-386.

76 L. Wu, J. Zheng, L. Wang, X. Xiong, Y. Shao, G. Wang, J.-H. Wang, S. Zhong and M. Wu, *Angew. Chem.,* 2019, **58**, 811-815.

77 L. Yan, J. Shu, C. Li, X. Cheng, H. Zhu, H. Yu, C. Zhang, Y. Zheng, Y. Xie and Z. Guo, *Energy Storage Mater.*, 2019, **16**, 535-544.

Journal Name ARTICLE

A new family of cation-disordered Zn(Cu)-Si-P compounds as high-performance anodes for next-generation Li-ion batteries

Wenwu Li,[a,b] Xinwei Li,*[,c] Jun Liao,[a] Bote Zhao,[b] Lei Zhang,[b] Le Huang,[a] Guoping Liu,[a] Zaiping Guo,[d] and Meilin Liu*[,b]

Keywords: Li-ion battery, Si-based anode, cation-disordered, Zn(Cu)-Si-P family

Table of Content

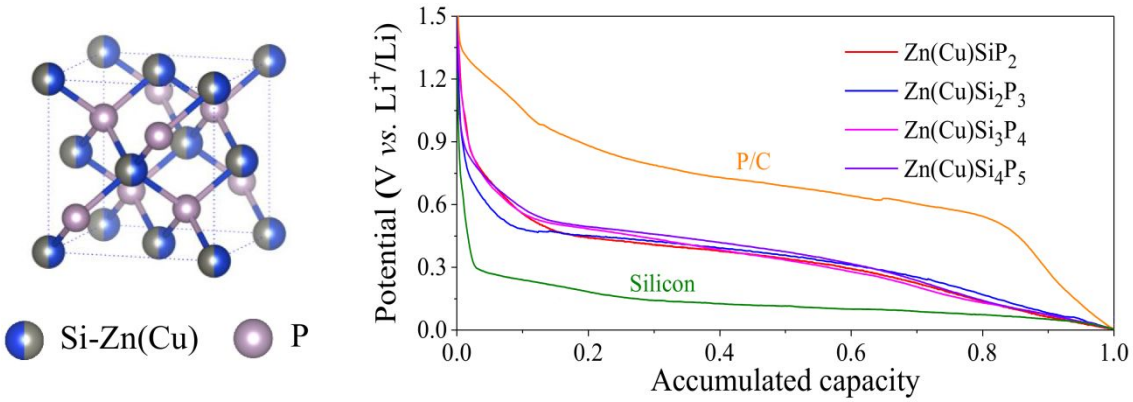

Cation-disordered compounds in the Zn(Cu)-Si-P family demonstrate better Li-storage performance than the cation-ordered $ZnSiP_2$ phase due largely to faster electronic and ionic conductivity and better tolerance to volume change during cycling, as confirmed by first-principles calculations and experimental measurements.

Broader context

Developing low-cost, high-performance anodes for Li-ion batteries to replace the widely used graphite electrode is highly desirable to meet the ever-increasing demands for large capacity, high-rate capability, and long cycling life. Recently, anodes based on multi-phase composites have achieved improved energy density, cycling life, and rate performance than those binary- or unary phase materials (*Energy Environ. Sci.*, 2017, **10**, 1456-1464). Further, the constituent phases of the composites show reversible synergistic effect during charge/discharge cycles. However, the synthesis of these complex compounds still faces the challenge of limited thermodynamic stability of the materials. Therefore, rational design of multi-phase materials with excellent electrochemical performance as well as cost-effective synthesis procedures is of great value to the development of a new-generation Li-ion batteries.